Materials Science & Engineering A 781 (2020) 139228

Contents lists available at ScienceDirect

Materials Science & Engineering A

journal homepage: http://www.elsevier.com/locate/msea

Determining volume fractions of γ, γ′, γ″, δ, and MC-carbide phases in Inconel 718 as a function of its processing history using an advanced neutron diffraction procedure

Nicholas C. Ferreri [a], Sven C. Vogel [b], Marko Knezevic [a,*]

[a] Department of Mechanical Engineering, University of New Hampshire, 03824, Durham, NH, USA
[b] Materials Science & Technology Division, Los Alamos National Laboratory, 87545, Los Alamos, NM, USA

ARTICLE INFO

Keywords:
Phase composition
Precipitates
Neutron diffraction
Additive manufacturing
Inconel 718

ABSTRACT

In this work, quantitative crystallographic and microstructural analyses of γ, γ′, γ″, δ, and MC carbide phases are performed on wrought samples, samples fabricated via additive manufacturing (AM), and samples that underwent hot isostatic pressing (HIP) after AM of alloy Inconel 718 (IN718). In doing so, an advanced neutron diffraction-based procedure is developed facilitating the determination of volume fractions of every detectable phase in the alloy. To supplement the diffraction procedure, precipitate sizes are measured by scanning electron microscopy. Moreover, semi-quantitative elemental analyses are performed by energy dispersive spectroscopy. Finally, image thresholding is carried out on micrographs of samples that underwent cathodic dissolution to create secondary electron contrast between phases to verify the phase fractions determined from the neutron diffraction datasets. The study reveals a significantly higher volume fraction of δ phase and a significantly lower volume fraction of γ″ phase governing a higher strength of the AM material relative to the lower strength AM + HIP and wrought materials. Furthermore, γ′ and MC volume fractions are found similar in the materials despite the differences in MC morphology, elemental composition and distribution controlling the dispersion strengthening. These results are presented and discussed in this paper along with the procedure developed for determining volume fractions of all detectable phases present in the alloy.

1. Introduction

Inconel 718 (IN718) is a nickel-base superalloy with high static strength and excellent resistance to creep and rupture at elevated temperatures [1]. Its superior corrosion and oxidation resistance makes it a desirable container material for molten salt reactors [2] as well as a material for rocket motors and for blades, disks, shafts, and fasteners in industrial gas turbines and jet engines [1,3–6]. IN718 is traditionally cast, wrought, or sintered, but through additive manufacturing (AM) it is possible to produce end-use parts with complex geometries that would be impossible or expensive with traditional manufacturing [4,7–12]. It has also been observed that despite the sub-optimal weld-like microstructures created as a product of AM, quasi-static mechanical properties are often favorable in AM material as compared to their cast or wrought counterparts [13–18]. This makes AM an attractive processing pathway, and as a result there is considerable research being done to make connections amongst AM processing parameters, microstructure, phase content, and mechanical properties [13,15,19–22]. This work focuses on understanding the extent to which AM affects the phase composition of IN718 and how that may influence mechanical properties.

Depending on elemental composition, solidification, and heat-treatment conditions, several phases can coexist within IN718. These phases have specific crystal structures and elemental compositions (Table 1). The primary phase is the austenitic γ phase, which is a face-centered cubic (fcc) Ni–Fe–Cr solid solution. γ is strengthened through substitutional and interstitial alloying (primarily with Mo, Mn, and C, respectively), which creates localized lattice strains that impede dislocation motion [1,23]. Phases in718 that are not γ are considered secondary, and these secondary phases have major, but varying effects on material strength depending on their morphology, chemistry, distribution, and interface coherency [1]. Phases with incoherent particle-matrix interfaces are not shearable and will locally halt slip,

* Corresponding author. at: University of New Hampshire, Department of Mechanical Engineering, 33 Academic Way, Kingsbury Hall, W119, Durham, NH, 03824, USA.
E-mail address: marko.knezevic@unh.edu (M. Knezevic).

https://doi.org/10.1016/j.msea.2020.139228
Received 24 January 2020; Received in revised form 9 March 2020; Accepted 9 March 2020
Available online 12 March 2020

Table 1
Phases in Inconel-718. Primary composition indicates major elemental constituents.

	Phase	Crystal System	Space Group	Primary Composition
Solid Solution Matrix	γ	Cubic	Fm-3m	Ni,Cr,Fe – Based
Intermetallic	γ′	Cubic	Pm-3m	Ni_3(Ti,Al,Nb)
	γ″	Tetragonal	I4/mmm	Ni_3(Nb,Ti)
	δ	Orthorhombic	Pmmn	Ni_3(Nb,Ti)
Topographically Close-Packed (Intermetallic)	η	Hexagonal	P63/mmc	Ni_3(Ti,Al)
	Laves	Hexagonal	P63/mmc	(Ni,Cr,Fe)$_2$(Nb,Ti)
Carbide	MC	Cubic	Fm-3m	(Nb,Ti) (C,N)
	$M_{23}C_6$	Cubic	Fm-3m	(Cr,Fe)$_{23}$C$_6$

which causes dislocations to deflect around a particle or form Orowan loops [23]. This type of strengthening is highly dependent on particle size and particle dispersion, which have an inverse and direct correlation, respectively, to material strength [24]. Incoherent phases observed in different IN718 alloys include the intermetallic δ, η, and Laves phases as well as various carbide phases such as MC and $M_{23}C_6$ (M = metal, C = carbon) [1]. These incoherent phases can help refine grain size, but when exceedingly coarse and acicular they will be detrimental to mechanical performance by offering less dispersion hardening and, if located at grain boundaries, will impede grain boundary sliding, which reduces ductility but may improve creep resistance [1,25,26]. Secondary phases with coherent or semi-coherent particle-matrix interfaces provide the greatest contribution to hardening in718. These are the ordered cubic γ′ ($L1_2$) and body-centered tetragonal (bct) γ'' ($D0_{22}$) phases with primary compositions of Ni_3(Al,Ti,Nb) and Ni_3(Nb,Ti), respectively [1,26,27]. Elemental compositions are listed for all phases in Table 1 [1,28–33]. Like all precipitates, γ′ and γ'' form during heating of the super-saturated fcc γ phase, where increased solute mobility allows for localized elemental segregation. The γ'' phase, however, is metastable at room temperature and can transform from bct into an orthorhombic δ phase (Ni_3(Nb,Ti)) during periods of prolonged heating or exposure to sufficiently high temperatures [34]. The high coherency strain energy resulting from misfit lattice parameters/crystal structures in addition to the creation of antiphase boundaries (APBs) in γ′ and γ'' precipitates when sheared by dislocations, provide a large increase in slip resistance given the nanoscopic particle size and fine dispersion of these phases [24]. Moreover, the γ'' phase has a coherent disc-like morphology with {100} habit plane and is associated with greater strengthening than γ′ due to the greater coherency strain created from the elongated c-axis of the γ'' unit cell and greater APB energy [31,35]. Because strengthening in cast or wrought IN718 is highly dependent on secondary phase content/morphology and precipitation is affected by solute concentrations, solidification rate, and heat treatments, AM IN718 can have vastly different microstructures and phase compositions. The effect of AM and precipitate size on the strength of IN718 has been studied [36–38]; however, the complete phase composition of AM IN718 with differentiated γ, γ′, γ'', δ, and carbide phases, has never been quantified. Due to size and crystallographic texture, there is inherent difficulty in the quantitative characterization of these secondary phases using characterization techniques such as electron microscopy and X-ray diffraction. Moreover, these characterization techniques focus on phase identification, confirming presence and morphology, but not on determining statistically significant volume fractions [39]. As a result of the inherent difficulties, there is significant scatter over the literature in reported phase data with no single report on a complete characterization of phase fractions in alloy IN718. Alternatively, the low neutron attenuation by most elements makes it possible to probe up to several cm^3 of material during neutron diffraction, which is impossible with X-rays or electrons. The technique allows for the analyses of bulk microstructural characteristics, which are especially important given the inhomogeneous microstructures in718, especially manufactured by AM.

In this study, a neutron diffraction-based procedure is developed that uses microstructural measurements made via scanning electron microscopy to ensure robust Rietveld analyses of IN718 diffraction data enabling the evaluation of γ, γ′, γ'', δ, and MC volume fractions. Advantages of neutron diffraction include the large neutron scattering cross-sections of Fe (11.22 b coherent elastic scattering cross-section), Ni (13.3 b) and Nb (6.253 b) atoms, which boosts signal/noise for most secondary phases, which have high at-% Ni and/or Nb. Moreover, the differences in neutron scattering cross-sections between Nb, Ti, and Al make it possible for elemental refinement within ordered phases when performing Rietveld refinements on neutron diffraction data [40]. This allows for more accurate refinements, which would be difficult to achieve with X-ray diffraction datasets due to the relatively similar photon scattering cross-sections between Ni, Nb, Ti, and Al [41]. Consequently, it is demonstrated that the developed methodology in conjunction with precipitate characterization via scanning electron microscopy facilitates the phase fraction determination of all primary phases present in the alloy with high accuracy.

Neutron diffraction measurements are taken for IN718 samples in the AMS 5663 standard heat treatment condition created by AM, hot-isostatic pressed (HIP) following AM, and wrought. The purpose is to study the effect of AM and HIP on the phase composition of IN718, in comparison to wrought IN718, and establish relationships between phase fractions and mechanical behavior of the alloy. The collection of high-intensity neutron diffraction data specifically allows for accurate crystallographic texture, crystallite/grain size, and lattice parameter gradient (microstrain) measurements of secondary phases. This enables the quantification of material phase composition by implementing a series of Rietveld refinements. Scanning electron microscopy (SEM) is performed to estimate precipitate sizes, energy dispersive spectroscopy (EDS) is performed to obtain semi-quantitative elemental analyses on various precipitates, and image thresholding is performed on micrographs of samples that underwent cathodic dissolution to create secondary electron (SE) contrast between phases. These are performed to either provide compositional information for phase models during the Rietveld analysis of neutron diffraction data, or to support the volume fraction determinations from the diffraction data. Although transmission electron microscopy would have been more appropriate for phase/precipitate identification, the EDS data collected is found to be sufficient. The study determines a variation in the volume fractions of δ and γ'' in the AM material as compared to the AM + HIP and wrought materials. Moreover, all γ′ and MC volume fractions were relatively similar despite the differences in MC morphology, distribution, and elemental composition. The quantitative data acquired in the present work can be used in polycrystal plasticity modelling [42–46], which can provide further insight into the deformation micro-mechanics for microstructural design of the alloy IN718 [47].

Table 2
Elemental composition for IN718 powder as received by supplier.

	Ni	Cr	Fe	Nb	Mo	Ti	Mn	Si	Cu	Al	C	S	P	B
wt-%	55.5	18.2	14.9	5.5	3.3	1.15	0.35	0.35	0.3	0.3	0.08	0.015	0.015	0.006
at-%	54.9	20.3	15.5	3.4	2.0	1.39	0.37	0.72	0.3	0.7	0.39	0.027	0.028	0.032

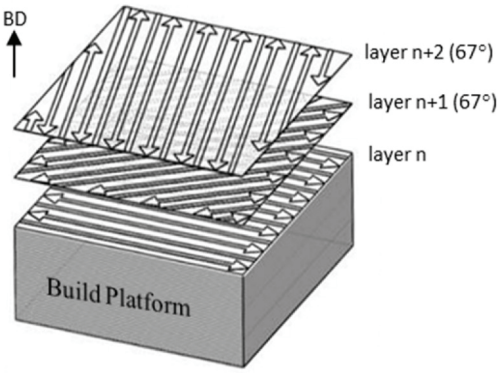

Fig. 1. Schematic showing laser path, which rotates 67° for each new layer of powder with respect to the previous layer during the laser powder bed fusion of IN718. Build direction is indicated as BD.

2. Experimental methods

2.1. Material and sample preparation

Additively manufactured samples made for tensile testing in studies by Gribbin et al. [23] and Ghorbanpour et al. [24] were used for all experimentation in the current work. Detailed descriptions of the AM process and both AM and wrought IN718 samples can be found in those works, while only brief descriptions of material processing and sample manufacturing is provided here. AM bars were fabricated from a metallic IN718 powder supplied by Electro Optical Systems (EOS) using the laser powder bed fusion (LPBF) technique [48]. The elemental composition of the powder is provided in Table 2, which had particle diameters ranging from <1 μm to 80 μm with a mean diameter of 35 μm. The EOS LPBF IN718_Performance 1.0 parameter set (2014) was used for LPBF sample processing, which utilizes a 285.0 W laser with a scan speed of 960 mm/s. Powder layer thickness was approximately 40 μm and laser path was rotated 67° counterclockwise, as shown in Fig. 1, after each cycle of lasering/powder re-coating.

AM and wrought tensile specimens were initially manufactured/wrought as bars then were subsequently machined to meet ASTM-E9 specifications (flat "dog bone" samples of 3 mm thickness, 6 mm width in the gage section, and a gage section length of 25 mm). Initial bars were oversized so that >1 mm of material could be removed from all free surfaces. Once machined, some of the AM samples underwent a 4 h period of HIP at 1163 °C under 100 MPa to reduce internal porosity, which is often relatively high in AM materials [49]. Prior to characterization, all samples endured a final AMS 5663 heat treatment. This multi-step treatment consists of an initial 1 h solution treatment at 954 °C followed by fan cooling in Ar to 120 °C then a double-aging treatment. The aging procedure involves holding samples at 718 °C for 8 h, furnace cooling (50 °C/h) to 621 °C, holding for an additional 8 h, then air cooled to room temperature. The objective of AMS 5663 is to relieve residual stress and increase γ'' precipitation to maximize material strength [50]. The wrought samples of IN718 with the same nominal composition were cut from a shaped forging and heat treated per AMS 5663. Material from a heat-treated wrought tensile sample and from heat-treated LPBF and LPBF + HIP tensile samples manufactured with their loading axes parallel to the LPBF build direction (BD) were used for neutron diffraction experimentation and scanning electron microscopy.

2.2. Characterization by electron microscopy

Samples were prepared for microscopy using standard metallographic techniques. Initially, specimens were ground with 180, 240, 400, 600, and 1200 grit silicon carbide (SiC) abrasive paper and subsequently polished with aqueous 0.5 μm and 0.05 μm alpha alumina (Al_2O_3) suspensions on a non-abrasive soft cloth [51–53]. Final polishing was done with an aqueous 0.02 μm colloidal silica (SiO_2), also on a non-abrasive soft cloth. SE images were taken on a Tescan Lyra 3 GMU field emission scanning electron microscope (SEM) to observe phase morphology and distribution on polished samples. The SEM was also used to perform EDS on polished samples. Characteristic X-rays were generated by an incident electron beam with an energy of ~16 keV and spot diameter (on sample surface) of ~30 nm. X-ray collection time was 120 s/scan, and characteristic spectra were analyzed in the EDAX TEAM software using the eZAF algorithm for quantitative compositional analysis [54]. Lower electron beam energies are more appropriate when performing EDS on small features due to decreased electron penetration depth; however, it was necessary to maintain a relatively high beam energy in order to excite enough L_α electrons in Fe, Ni, and Cr atoms to produce sufficient X-rays for quantitative analysis.

A few samples sectioned from the heat-treated and polished tensile bars received an additional electrolytic surface treatment prior to SE imaging. A technique devised by Radavich [55] whereby a 25 V potential was applied to an electrolytic cell that used an IN718 cathode and a 1:4 by volume sulfuric acid (H_2SO_4)-methanol (CH_3OH) electrolyte solution was used to perform selective electrolysis on δ, γ′, and γ'' phases. The cathodic dissolution of δ, γ′, and/or γ'' precipitates created topographical holes in the IN718 surface that appeared dark in SE imaging with respect to the γ phase. Other phases that remained in relief accumulated charge when viewed with SE and appeared white. By converting SE micrographs of the electrolytically prepared IN718 to grayscale in Matlab and then to black and white, a contrast threshold could be applied to segregate light from dark phases. The ratio of dark or light pixels to total pixels represents the area fraction of the respective phase(s).

2.3. Experimentation by neutron diffraction

Neutron diffraction experimentation was performed on the time-of-flight (TOF) high-pressure-preferred orientation (HIPPO) neutron diffractometer [39] at the pulsed neutron source of the Los Alamos Neutron Science Center (LANSCE) [56]. Pieces of IN718 tensile samples were glued on Cd-wrapped Al sample holders. Using a robotic sample changer [57], each sample was exposed to an incident neutron beam collimated to 10 mm diameter for ~60 min at an average proton current of 100 μA. LPBF and LPBF + HIP samples were orientated such that the build direction was perpendicular to the incident neutron beam. In total, 132 histograms were obtained from three different sample orientations (0°, 67.5°, and 90°) for the five HIPPO detector rings with nominal diffraction angles of 150°, 120°, 90°, 60°, and 40°. The 132 histograms were used to calculate an orientation distribution function (ODF) and were also integrated to create single histograms for each neutron diffraction angle that are largely free from texture influence (due to HIPPO's large detector coverage). Therefore, texture effects were assumed negligible on these integrated histograms, which allowed for quantitative phase fraction determination using the Rietveld method. Moreover, the resulting threefold increased period of neutron exposure, as well as integration of the data of each ring, greatly increased the statistical quality of the data compared to individual histograms used for the ODF calculation. This allowed for the ability to resolve the low volume fraction phases in the IN718 samples.

3. Neutron diffraction data analysis

The Maud diffraction analysis software was used to evaluate all experimental neutron diffraction histograms. The models governing calculated diffraction histograms in Maud are described in Refs. [39, 58–61] and incorporate effects of sample geometry, instrumentation, and material structure on the intensity and shape of Bragg reflections. The effects of variations in crystallographic properties, texture, and phase composition on the intensity of a given diffracting plane are

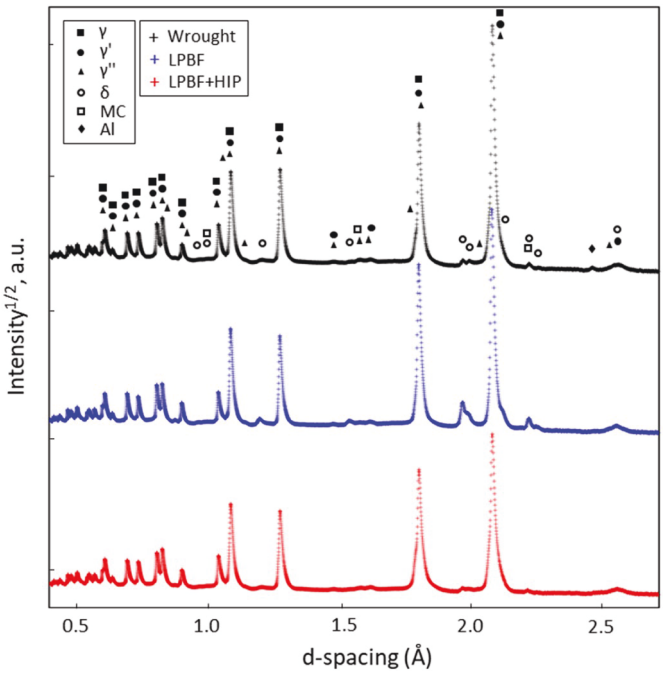

Fig. 2. Experimental neutron diffraction histograms from the 150° detector bank for LPBF, LPBF + HIP, and Wrought IN718. Bragg reflections for all detected phases are labeled except for those with low d-spacings or intensities near background, which were omitted to enhance plot readability. Metallic aluminum (Al) reflections were seen because of neutron beam interaction with Al sample holders, which resulted in the detection of Al-diffracted neutrons in the 150° and 120° detector banks.

captured by the physics-based diffraction models used in Maud [58, 60–67].

The integrated experimental neutron diffraction histograms were fit by calculating the diffraction contribution for each phase observed in each sample. The Rietveld method was applied whereby the relevant crystallographic and scaling parameters of all phases were refined to increase the quality of the least-squares fit between calculated and experimental diffraction histograms. Bragg reflections corresponding to γ, γ′, γ′′, δ, and/or MC phases were observed in all 3 samples as seen in the experimental histograms in Fig. 2.

Prior to conducting the phase analyses, crystallographic parameters were determined for all phases via two series of Rietveld refinements. Both series were performed with three phases (γ, γ′, γ′′ or γ, δ, MC) on either LPBF or wrought datasets. This was done because each dataset is better suited for refining certain phases. For example, the LPBF dataset contains higher intensity δ reflections as compared to LPBF + HIP and wrought datasets. This makes for more robust peak fitting and is why the crystallographic parameters for δ were determined from the LPBF dataset. Using the same logic, γ′ and γ′′ crystallographic parameters were obtained from a Rietveld analysis of the Wrought dataset, and MC crystallographic parameters were obtained from a Rietveld analysis of the LPBF dataset. Once the crystallographic parameters for a phase was determined through refinement, they were assumed to be the same in all other samples. These parameters are shown in Table 3 along with other relevant crystallographic parameters that remained fixed throughout the refinements. Also, it should be noted that the only refined crystallographic parameter for the γ phase was microstrain, which was identical in all samples (within the calculated uncertainties).

The Rietveld refinements were all performed in a similar manner when determining the crystallographic parameters in Table 3. First, a 4th order polynomial was used to fit the backgrounds of each histogram (corresponding to each detector bank) and their coefficients were always being refined throughout the Rietveld analysis. The DIFC parameter was also continuously refined for all histograms, and because the γ lattice parameter was fixed, based on the value determined by Mukherji et al. [32], the γ lattice parameter acted as an internal standard when refining lattice parameters for all other phases. The initial lattice parameters (excluding γ) and atomic partial occupancies were set based on literature values [29–33] then subsequently refined. Despite the possibility of slight Ti solubility at the 0,0,0.5 atomic site in δ, Ti was not included nor was the partial occupancy refined due to instability in the refinement when included. Additionally, it was noted that γ′′ can be no more than ~5 at-% Ti at the 0,0,0 atomic site because more than this amount would unreasonably increase the intensity of the γ′′ reflection at the d-spacing of ~5.25 E.

Microstrains (which contribute to peak broadening) were refined after being initially set to the default 6×10^{-4} με, which assumes little-to-no effect on peak broadening. Precipitate equivalent diameters for all phases were approximated from measurements made using scanning

Table 3
Final phase parameters (both fixed and refined) for the analysis of neutron diffraction data in Maud. These values were used for all samples (LPBF, LPBF + HIP, and Wrought) unless specified otherwise.

Phase	Lattice Parameter (Å)	Crystallite Size (nm)	Microstrain (με)	Space Group	Atomic Site Properties		
					Location (x, y, z)	Partial Occupancy	B_{iso} (Å^2)
γ	a = 3.598	>1000	0.00225[a] ±0.00003	Fm-3m	0, 0, 0	$Ni_{0.4}Cr_{0.3}Fe_{0.3}$	0.55
γ′	a = 3.612[a] ±0.001	15	0.00323[a] ±0.00222	*Pm*-3m	$0, \frac{1}{2}, \frac{1}{2}$	$Ni_{1.0}$	0.65
					0, 0, 0	$Al_{0.63}Ti_{0.37}$[a]	0.65
γ″	a = 3.571[a] ±0.001 b = 7.286[a] ±0.002	30	0.00156[a] ±0.00021	*I4/mmm*	$0, 0, \frac{1}{2}$	$Ni_{1.0}$	0.70
					$0, \frac{1}{2}, \frac{1}{4}$	$Ni_{1.0}$	0.70
					0, 0, 0	$Nb_{>0.95}Ti_{<0.05}$[a]	0.75
δ	a = 5.100[a] ±0.002 b = 4.226[a] ±0.002 c = 4.504[a] ±0.002	400[b] > 1000[c]	0.00270[a] ±0.00022	*Pmmn*	$\frac{1}{2}, 0, \frac{1}{6}$	$Ni_{1.0}$	0.75
					$0, \frac{1}{2}, \frac{1}{3}$	$Ni_{1.0}$	0.75
					$0, 0, \frac{1}{2}$	$Nb_{1.0}$	0.90
MC	a = 4.435[a] ±0.005	200[b] > 1000[c]	0.00363[a] ±0.00244	Fm-3m	0, 0, 0	$Nb_{0.81}Ti_{0.19}$[a]	0.185
					$\frac{1}{2}, \frac{1}{2}, \frac{1}{2}$	$C_{1.0}$	0.310

+/− resulting from histogram fitting uncertainty in Maud.
[a] Values determined via Rietveld refinement in Maud.
[b] Values used only for LPBF material.
[c] Values used only for LPBF + HIP and Wrought material.

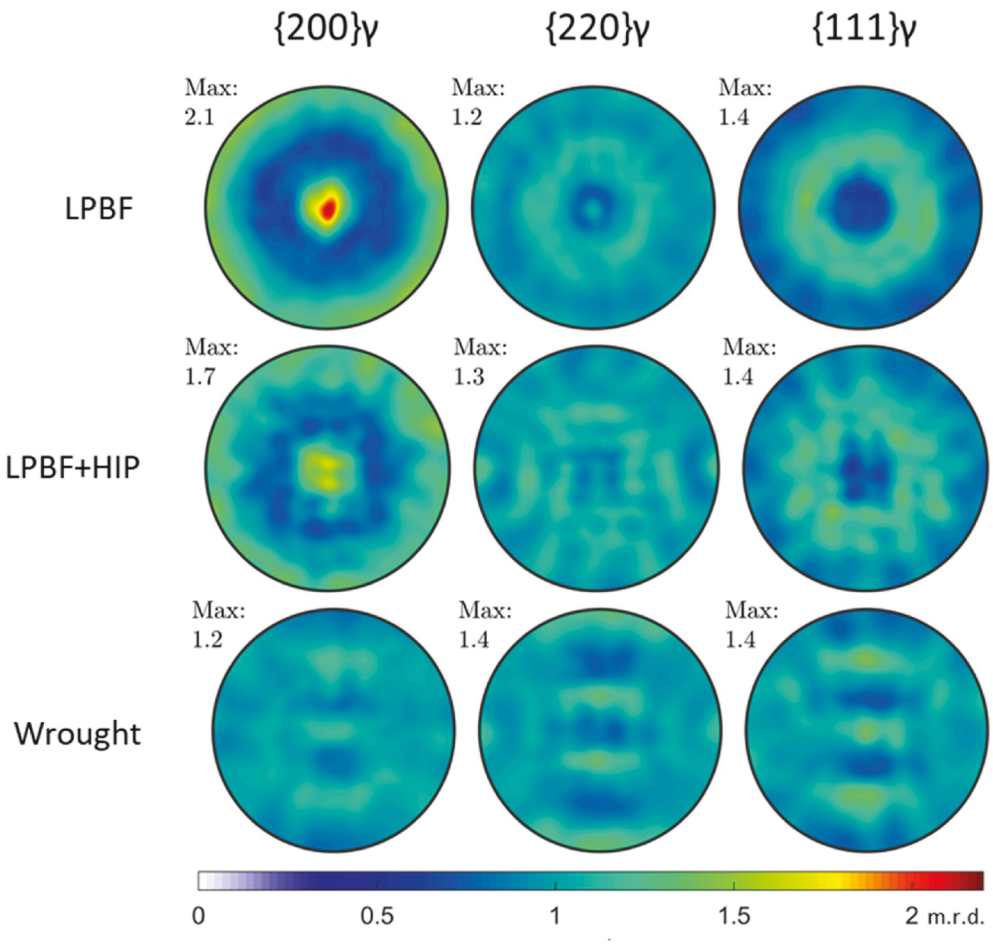

Fig. 3. Pole figures showing the crystallographic texture of the γ phase in LPBF, LPBF + HIP, and wrought IN718 samples. Pole figures were calculated from ODFs that were generated in Maud using the E-WIMV texture algorithm when performing full γ texture analysis on the 132 histograms from each IN718 neutron diffraction dataset. Build direction is out-of-plane in LPBF and LPBF + HIP pole figures, while rolling direction (RD) is vertical and transverse direction (TD) is horizontal for the shaped forging material. Pole density is plotted in units of multiple of a random distribution (m.r.d.).

electron microscopy and used as crystallite sizes for respective phases in Maud, which remained fixed throughout the refinement process. Although most phases had no noticeable variation in crystallite size between samples, δ and MC did have sample-unique sizes. Moreover, phases with greater than a 1000 nm crystallite size were marked as such and not measured because particle size broadening observed by neutron diffraction is negligible when crystallites are larger than ~1000 nm [68]. Additionally, because γ grains were very coarse and lacked intragranular dislocation structures (per EBSD), which would create low-angle sub-grain boundaries, it was assumed that mosaicity in γ grains was minimal and that mean crystallite size was also greater than 1000 nm. Atomic displacement parameters, B_{iso}, were also fixed during refinement, but were established based on literature values [69–71].

Initially, the only phase parameters being refined were scale parameters and lattice parameters. When these values reached a convergence, microstrain was refined followed by atomic partial occupancies for ordered phases. Refining partial occupancies for atomic sites that consist of solute elements (Nb/Ti/Al) adjusts for variations in the intensities of the diffracting planes that are partially comprised of these atomic sites. Because the scattering power of an atomic site is the weighted sum of all the elemental contributions, no more than two elements can be refined per site since otherwise there would be an infinite number of solutions to the refinement. This is why in the γ′ phase, for example, only Al and Ti were included in the partial occupancy refinement and γ′ was assumed to be Nb insoluble. Although the assumption made for the Rietveld analysis that no more than two elements can exist at an atomic site is not true in a strict sense, a two-element partial occupancy refinement (of elements with different scattering powers) still allows for the adjustment of hkl-specific reflections that have deviating intensities on account of variations in atomic site chemistries.

During Rietveld analysis, parameters were refined in series to allow for convergence through the least-squares fitting process. If heavily correlated variables are simultaneously refined, for example crystallite size and microstrain, which both contribute to the broadening of Bragg reflections, convergence would not occur [72]. Additionally, if too many slightly correlated variables are simultaneously refined, the chance for convergence is decreased. This also increases the risk of variables converging to non-physical values as a result of the refinement maximizing the quality of the fit. This occurs most often when fitting datasets of poor statistical quality; therefore, due to the low-intensity, broad, overlapping, or absent secondary phase peaks in the IN718 datasets, neither atomic displacement parameters nor crystallite sizes were refined [72].

Once the Rietveld refinements performed to determine crystallographic parameters were completed, a final series of refinements was carried out for each sample using these crystallographic parameters to determine phase composition. All phases were included in these refinements and only phase volume fractions were being refined.

A simultaneous Rietveld analysis of the 132 histograms was also performed to refine the ODF and quantify the texture of the γ phase. This full texture analysis was done in Maud using the E-WIMV texture algorithm and followed what was described in Wenk et al. [39]. Pole figures, which show the refined γ texture, are seen in Fig. 3. There are $\{200\}_{\gamma}$ fibers in the LPBF and LPBF + HIP material, but overall texture is weak. During the phase analysis, it was assumed that integrating the neutron diffraction data into five histograms would produce five datasets largely free from the influence of this texture. This was shown by Takajo et al. who performed these integrations and produced histograms with approximately (but not completely) random texture [73]. However, the slight influence of texture would be negligible in the IN718 integrated

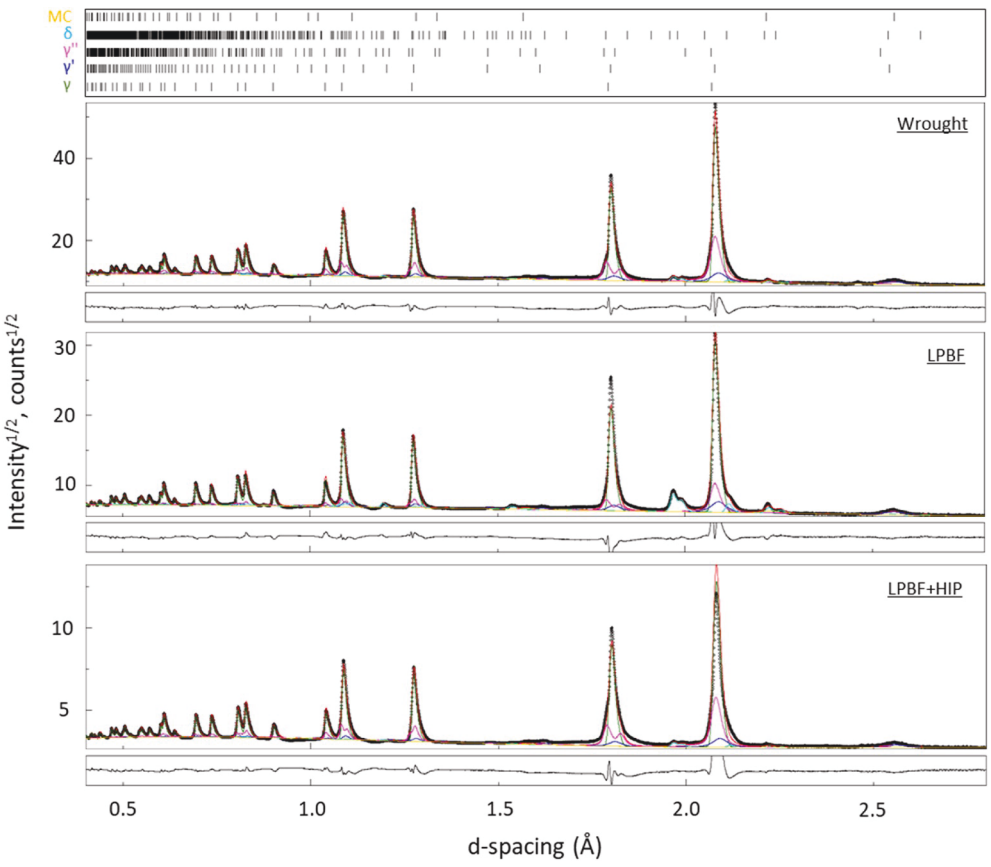

Fig. 4. Experimental and calculated neutron diffraction histograms for LPBF, LPBF + HIP, and Wrought IN718 data collected by the 150° detector bank. Rietveld fits are results from a series of 5-phase (γ, γ′, γ″, δ, and MC) refinements performed to model material phase composition. Each red histogram is a sum of all its constituent phase contributions, which are shown in various colors. Bragg reflection locations for all modeled phases are indicated, and difference curves representing variation between calculated histograms and experimental data are also shown. (For interpretation of the references to color in this figure legend, the reader is referred to the Web version of this article.)

Table 4
Phase composition as determined via neutron diffraction for LPBF, LPBF + HIP, and wrought IN718.

	γ	γ′	+/−	γ″	+/−	δ	+/−	MC	+/−
LPBF	bal	6.5	1.4	8.4	0.3	5.9	0.4	1.9	0.5
LPBF + HIP	bal	5.4	0.8	17.7	0.5	1.1	0.2	0.5	0.2
Wrought	bal	6.5	0.8	17.8	0.5	1.3	0.1	0.9	0.3

Units of vol-%.
+/− resulting from histogram fitting uncertainty in Maud.

datasets, because γ texture was weak in the LPBF, LPBF + HIP, and wrought IN718. This validates the decision to ignore texture effects when performing the phase analyses on the integrated datasets.

4. Results

4.1. Phase volume fraction determination

Fig. 4 shows the experimental neutron diffraction data and Rietveld fit for LPBF, LPBF + HIP, and wrought IN718 samples in addition to the locations of all potential Bragg reflections for all modeled phases. Most of the non-visible peaks in secondary phases are the result of low volume fraction, low multiplicity, and/or particle size broadening that causes extremely low intensities. The Rietveld refinements performed for these three datasets were done within a 0.4 Å to 2.7 Å d-spacing domain. Phase volume percentages resulting from the refinements are displayed in Table 4. LPBF + HIP and wrought materials had relatively similar phase compositions, which differed from the LPBF material. The LPBF material had significantly less of the strengthening γ'' phase (8.4 ± 0.3 vol-%) than the LPBF + HIP (17.7 ± 0.5 vol-%) and wrought (17.8 ± 0.5 vol-%) materials, but consisted of 5.9 ± 0.4 vol-% δ as opposed to the marginal 1.1 ± 0.2 vol-% and 1.3 ± 0.1 vol-% in both LPBF + HIP and wrought samples, respectively. γ′ content was similar in all samples when incorporating uncertainty: 5.4 vol-% to 6.5 vol-% (±0.8–1.4%), while MC was higher in LPBF at 1.9 ± 0.5 vol-% and slightly lower in LPBF + HIP and wrought at 0.5 ± 0.2 vol-% and 0.9 ± 0.3 vol-%, respectively.

Although the volume fractions of all these phases has never been simultaneously calculated, there are some studies that provide partial volume fraction information of IN718. A study by Li et al. measured 5.75 wt-% δ and 12.33 wt-% γ′+γ'' in a hot-rolled rod of IN718 that underwent the AMS 5663 heat-treatment [29]. This is similar to the phase composition of the LPBF material. Moreover, the γ′ and γ'' values in the LPBF + HIP and Wrought material lie near the speculated volume fractions of 0.04 and 0.15, respectively, according to Devoux et al. [74]. Additionally, δ has been observed at volume fractions between 0 and 0.20 depending on the heat-treatment and exact elemental composition [35,75].

4.2. Quantifying uncertainty

Uncertainty in phase composition values are a product of the least-squares fitting performed during the Rietveld refinements of calculated diffraction spectra in Maud. Uncertainty is higher for γ′ and γ''

Table 5
R-value and quality of fit parameters for the Rietveld analysis of LPBF, LPBF + HIP, and wrought IN718 neutron diffraction data in Maud.

	R_{wp} (%)	R_{exp} (%)	χ^2
LPBF	3.977	0.362	120.70
LPBF + HIP	4.129	0.377	119.95
Wrought	3.478	0.347	100.46

because, as seen in Fig. 4, the majority of γ′ and γ′′ diffraction peaks are largely indistinguishable from the high-intensity γ peaks. Uncertainty is high for the MC phase and for the δ phase in the LPBF + HIP and wrought material because the reflections belonging to these phases have low intensities and overlap reflections from other phases. Peak overlap, and low-intensity, broad peaks are difficult to fit and can result in higher uncertainties for refined phase parameters during Rietveld analysis [72]. Difference curves are more pronounced at higher d-spacings due to issues incorporating incident neutron intensity normalization and absorption as they are more pronounced for slower neutrons and lead to poorer fits.

The quality of a fit between calculated and experimental spectra is determined by taking the ratio between R_{wp} and R_{exp} values. This ratio is known as χ^2, and these R values correspond to the quality of the Rietveld refinement and the quality of experimental data, respectively. A χ^2 of unity represents a perfect fit and large values like those calculated for the three IN718 samples indicate the presence of systematic error; however, R_{wp} values of 3.5–4.1% (shown in Table 5) are low, which suggests the opposite. The issue is that the extended data collection period for each sample significantly reduced R_{exp} values to the exceeding low values of 0.3–0.4%. The increased counts corresponding to increased sample exposure time improving the quality of diffraction data, which allows for betting fitting, but results in seemingly worse discrepancy indices [76]. Therefore, high χ^2 values are expected given high quality datasets with exceptionally low R_{exp} and low R_{wp}, which is

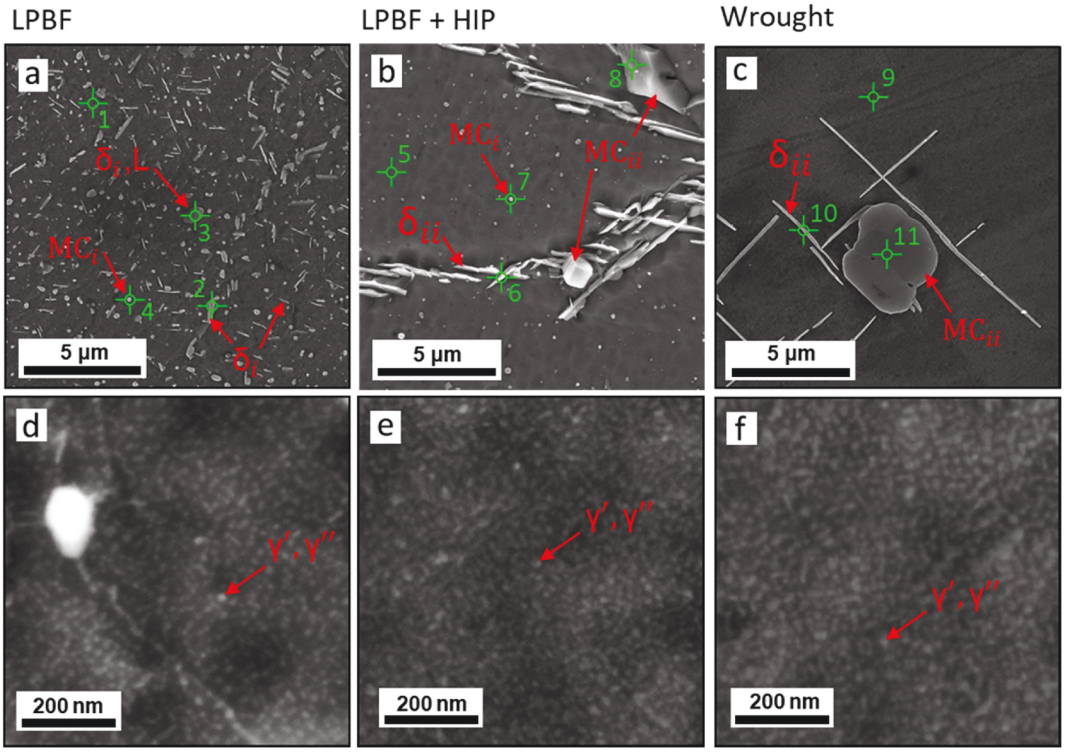

Fig. 5. SE micrographs of LPBF (a,d), LPBF + HIP (b,e), and Wrought (c,f) samples with both 25 μm and 1.0 μm view fields that reveal incoherent and coherent precipitate morphologies, respectively. Suspected precipitate phases are marked in red, and EDS spot scan locations are marked/numbered in green. (For interpretation of the references to color in this figure legend, the reader is referred to the Web version of this article.)

Table 6
Elemental compositions measured for various spots on LPBF, LPBF + HIP, and wrought IN718 samples using EDS. Suspected phases and potential compositions are tabulated based on EDS measurements and precipitate morphology observed in secondary electron micrographs.

EDS Spot	Sample	Composition (at-%)								Suspected Phase(s)
		Ni	Cr	Fe	Nb	Ti	Mo	Al	Si	
1	LPBF	48.0	22.4	23.6	2.4	1.3	1.3	0.8	0.2	γ, γ′, γ″
5	LPBF + HIP	51.8	22.4	19.4	2.5	1.5	1.6	0.7	0.1	γ, γ′, γ″
9	Wrought	53.3	21.9	18.4	2.6	1.5	1.5	0.7	0.1	γ, γ′, γ″
2	LPBF	56.9	16.6	16.6	5.8	2.3	1.2	0.6	0.1	δ_i
6	LPBF + HIP	63.4	13.0	11.1	8.3	2.9	1.0	0.2	0.1	δ_{ii}
10	Wrought	73.0	5.5	5.7	10.4	3.9	1.0	0.3	0.3	δ_{ii}
3	LPBF	54.3	18.3	18.7	5.4	1.7	1.1	0.5	0.1	δ_i or Laves
4	LPBF	35.8	20.1	22.2	12.6	0.5	5.8	0.5	2.7	MC_i
7	LPBF + HIP	47.4	22.0	18.1	8.7	2.3	1.0	0.5	0.0	MC_i
8	LPBF + HIP	9.2	6.2	4.2	61.0	17.9	0.3	1.0	0.3	MC_{ii}
11	Wrought	1.5	0.7	0.3	83.3	14.2	0.0	0.0	0.0	MC_{ii}

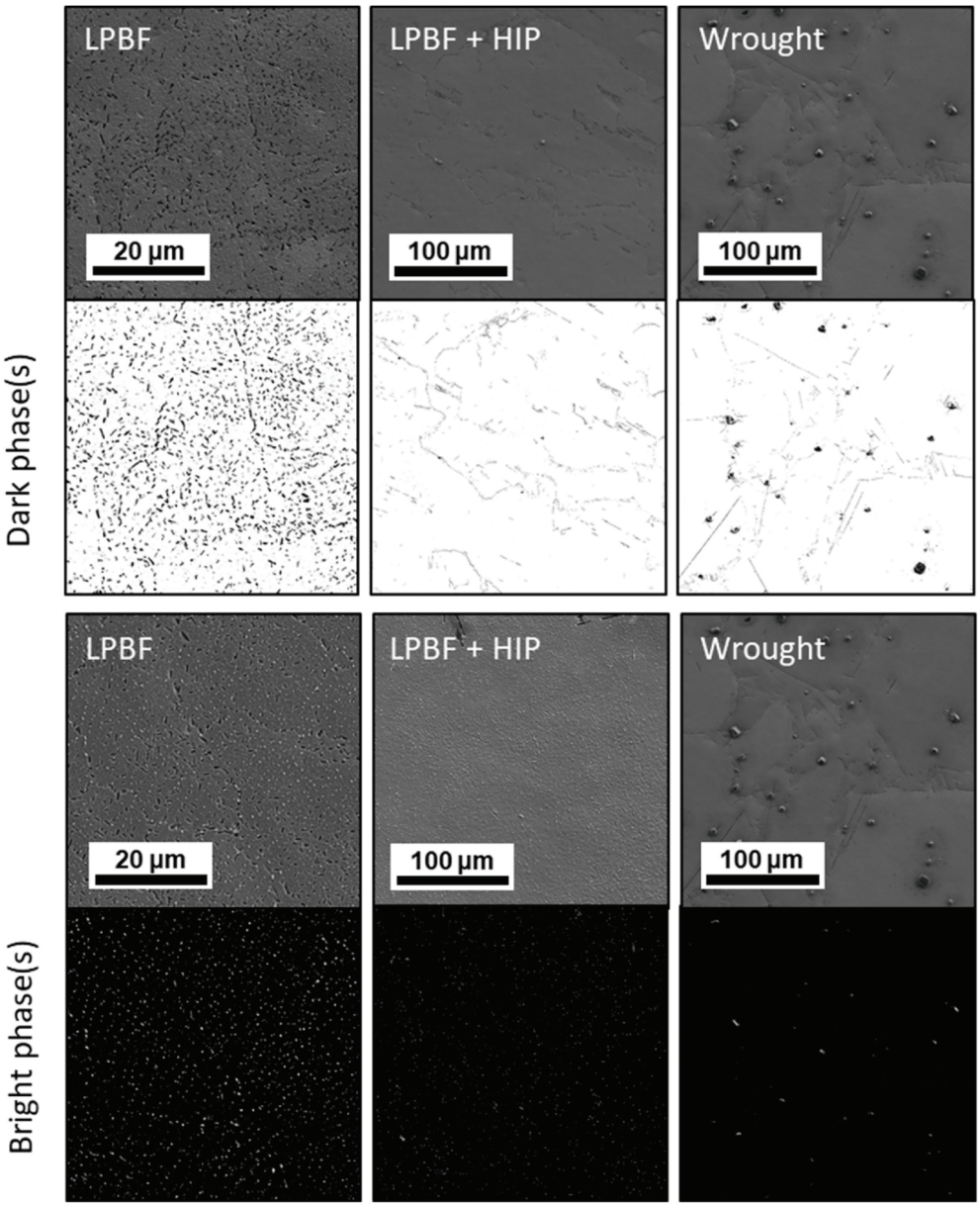

Fig. 6. Cathodic dissolution was used to prepare LPBF, LPBF + HIP, and Wrought IN718 samples to maximize contrast between the dark phase (δ and also MC in wrought) and the bright phases (MC and/or Laves) when imaging with SE.

what was observed in this study [76].

4.3. Microstructural analysis

Scanning electron microscopy was used to measure precipitate sizes, which were used to approximate crystallite sizes for phase models in Maud, and also to perform EDS on distinct precipitates in each sample, which supported the partial occupancy values for each phase resulting from the refinements. Fig. 5 shows two sets of SE micrographs corresponding to each sample with different view fields that highlight either large, incoherent precipitates or small, coherent precipitates. EDS spot scans were performed at points indicated by a green mark in Fig. 5, and the elemental composition calculated at each point is reported in Table 6. It is important to note, however, that the characteristic X-rays used for EDS are generated from up to 1 or 2 μm below the sample surface. Therefore, when performing EDS on very fine particles, it is possible that much of the material beneath is also being sampled. Because of this, EDS is semi-quantitative at small length-scales. Only relevant elements were included in the EDS analysis, and based on the results combined with observed precipitate morphologies, phase identities were inferred. Spot scans 1, 5, and 9 include γ, γ′, and γ′′ phases for LPBF, LPBF + HIP, and wrought samples and were used as baselines to compare other precipitate spot scans to.

IN718 samples underwent selective electrolysis to dissolve γ′, γ′′ and δ, which would leave topographical holes that would appear dark via SE imaging. This would leave the MC and Laves phases in relief causing them to build charge when viewed with SE and appear white. By converting the SE micrographs of the electrolytically prepared IN718 to grayscale in Matlab then to black and white, a contrast threshold could be applied to segregate phases appearing light (Laves, MC) from those appearing dark (γ′, γ′′ and δ). This can be seen in Fig. 6. Since γ′ and γ′′ cannot be observed at the magnifications used for imaging (50 and 250 μm fields of view), the phases segregated by image thresholding are δ (black) and MC/Laves (white). The results are shown in Table 7 and agree with the volume percentages determined by neutron diffraction. In addition to providing validation, the thresholding shows potential

Table 7
Phase composition as discernible via image thresholding using SE micrographs for LPBF, LPBF + HIP, and wrought IN718.

	γ, γ′, γ″	δ	MC, Laves
LPBF	balance	6.5 (1.5)	1.8 (0.8)
LPBF + HIP	balance	0.8 (0.2)	0.7 (0.2)
Wrought	balance	1.0 (0.5)	0.9 (0.6)

Units of area-%.
+/− resulting from uncertainty during thresholding is reported in parentheses.

Table 8
Solvus temperatures determined from other studies for relevant phases in AM IN718.

Phase	Solvus Temperature (°C)
γ′	900-970 [34,77]
γ″	910-930 [34,77,78]
δ	990-1020 [79,80]
MC	1040-1200 [79,81]
Laves	1010 [79]

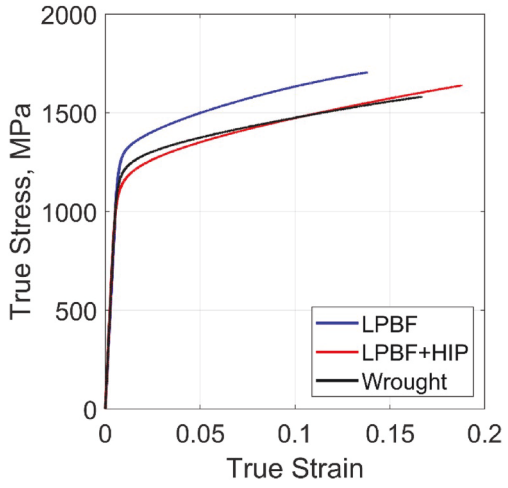

Fig. 7. True stress-strain behavior of LPBF, LPBF + HIP, and wrought IN718 in simple tension [86].

evidence of up to ~1 vol-% Laves in the LPBF material. Uncertainty reported for the volume percentages calculated from image thresholding are a result of accidental indexing of incorrect phases. Parts of MC particles, for example, appear dark in LPBF + HIP and wrought samples when they are assumed to be white, and charge buildup occurs at the edges of some holes in all samples, which appear white and create false MC/Laves counts.

5. Discussion

5.1. Phase confirmation

A validation of the neutron diffraction data was performed using electron microscopy. In particular, SE contrast thresholding is used to approximate certain phase volume fractions (see Table 7) and EDS is used to correlate phases with precipitate morphologies and distributions (see Fig. 5). EDS spot scans #2, #6, and #10 confirm the presence of δ in all samples. The δ precipitates observed in wrought and LPBF + HIP materials, δ_{ii}, are coarse, acicular, and nucleated at grain boundaries, which suggests a transformation of γ directly to δ_{ii} during heat treatment [31,35]. δ precipitates observed in the LPBF material, δ_i, were still acicular, but smaller and existed both within grains and at grain boundaries. EDS spot scans for δ in all samples (spot scans #2, #6, and #10) had elevated Ni and Nb and showed some Ti solubility. Less Ni, Nb, and Ti were observed in the δ_i EDS spot scan (spot scan #2 on LPBF sample) because the smaller particle size resulted in sampling much of the material beneath the precipitate. The elevated Ti in δ_i relative to Nb may be evidence that δ_i transformed from γ via the metastable, more Ti-soluble γ'' phase in the LPBF material. This is supported by the lower volume percent of γ'' observed via neutron diffraction in the LBPF sample as compared to wrought and LPBF + HIP samples (8.4 wt-% to 17.7 wt-% and 17.8 wt-%, respectively).

EDS spot scan #3 could be either δ_i or Laves based on elemental composition and morphology. Its shape is elongated, but also globular, which has been reported for both AM δ and Laves phases [31,79]. The composition calculated from this scan is similar to δ_i except that there is slightly elevated Cr and Fe and decreased Ni and Ti, which is slightly suggestive of Laves [81]. Although Laves was not detected in the neutron diffraction data, if its volume fraction was approximately less than 1% then it is possible that its Bragg reflections had such low intensity they were hidden in background or behind the reflections of other phases. Other studies [27,28,82] have reported Laves in as-built AM IN718, and because the solvus temperature for the Laves phase is approximately 1010 °C, as seen in Table 8, Laves particles would not have dissolved during ASM 5663 heat treatment if they had formed during LPBF [81]. The LPBF + HIP and wrought samples, showed no evidence via SE imaging and EDS of Laves phases. The HIP treatment solutionized the Laves and δ_i phases while δ_{ii} and MC_{ii} (coarse MC precipitates in wrought and LPBF + HIP material) precipitated at grain boundaries during the ASM 5663 heat treatment. Moreover, δ_{ii} and MC_{ii} grew coarse due to the prevalence of Nb in solid solution resulting from Laves and δ_i dissolution during HIP. The coarse, intergranular MC_{ii} detected in LPBF + HIP and wrought samples had high Nb content and raised Ti. A much smaller MC carbide, MC_i, was only observed in LPBF and LPBF + HIP samples. These carbides were not dissolved during the HIP treatment due to high solvus temperatures (approximately 1140°C–1200 °C) as seen in Table 8. EDS quantification shows elevated Ni, Nb, and Ti, but due to the small particle size these values are much lower that the calculated values for the larger MC_{ii}. However, since MC is the first secondary phase to precipitate from liquid during the solidification of IN718, it is affected by solidification segregation elements Mo and Si resulting in higher contents of these elements with respect to other phases [27,81,83–85]. Because the LPBF MC_i have elevated Mo and Si, the precipitate was correctly identified as MC. EDS was not performed on γ′ and γ'' precipitates because they could not be spatially resolved given the electron beam parameters used for EDS.

A mass balance calculation was performed to make sure the phase compositions determined via neutron diffraction analysis were plausible given the global solute element concentrations. Using the elemental composition provided for the IN718 powder and the phase stoichiometries determined from the Rietveld refinement, a mass balance calculation was performed. When allowing for minor deviations in stoichiometry due to potential Nb, Ti, and Al solubilities in all phases, and when taking into account the phase volume percent uncertainties, the phase compositions produced as a result of the refinements are all plausible.

5.2. Effect of phase composition on material strength

The true stress-strain behavior of the studied LPBF, LPBF + HIP, and wrought IN718 in simple tension was investigated in Gribbin et al. [86] and is shown in Fig. 7. It is unusual that the LPBF material has the highest strength despite having the lowest volume fraction of γ″, which suggests the presence of other strengthening mechanisms. Compared to the other material conditions, the LPBF material had a higher density of small ~200 nm MC_i precipitates, which would contribute to dispersion strengthening where dislocations are impeded and deflect around the non-deformable carbide particles during deformation [23]. That being said, it would be implausible for carbide dispersion to provide more of a

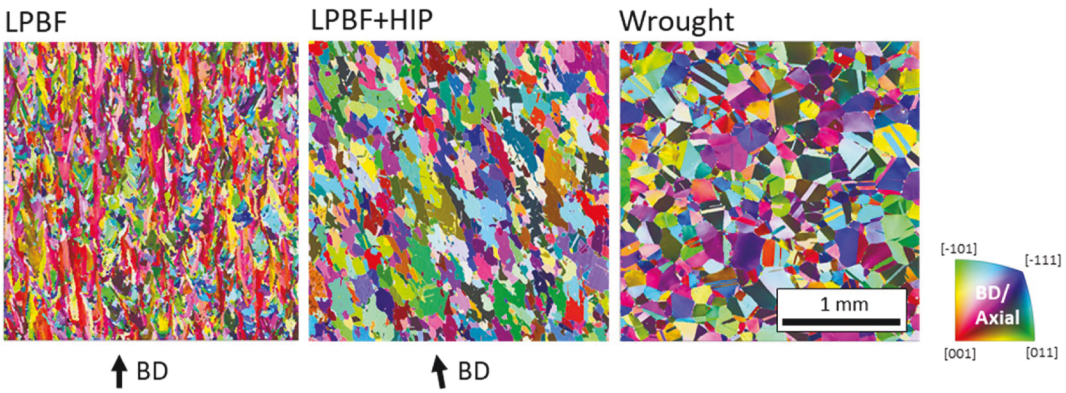

Fig. 8. Inverse pole figure (IPF) maps, with respect to BD, are shown for LPBF, LPBF + HIP, and wrought IN718. Maps were created from EBSD data [86] and the colors in the maps represent the orientation of the sample axis with respect to the local crystal lattice frame according to the IPF color key where BD or Axial directions are out of plane. The axial direction refers to the axis of the shaped forging. The 1 mm scale bar applies to all maps. (For interpretation of the references to color in this figure legend, the reader is referred to the Web version of this article.)

barrier to slip than the coherency hardening associated with γ''; therefore, this cannot be the only contributing factor to the increase in strength of the LPBF sample.

Inverse pole figure (IPF) maps [86] of the studied LPBF, LPBF + HIP, and wrought IN718 are shown in Fig. 8 and illustrate the grain structure of each sample. The wrought material has large, equiaxed grains that resulted from equilibrium cooling conditions and the LPBF + HIP material recrystallized during the HIP procedure resulting in a coarse microstructure, relative to the LPBF material. The typical weld-like microstructure seen in LPBF alloys is seen in the LPBF IN718 with many grains elongated towards BD surrounded by groups of smaller grains. This is due to the cyclic heating associated with AM, but could also be due to the high volume fraction of δ_i in the LPBF sample, which prevented grain growth via grain pinning [23,87]. Due to the large differences in grain size amongst samples, the finer-grain structure in the LPBF IN718 material is rationalized to govern the observed increase in strength, consistent with the Hall-Petch relationship [88].

6. Conclusions

This work has examined the phase fractions for LPBF, LPBF + HIP, and wrought IN718, which were determined by performing a series of multi-phase Rietveld refinements on neutron diffraction data. To this end, a novel neutron diffraction-based procedure is developed to simultaneously determine γ, γ′, γ'', δ, and MC phase volume percentages. The procedure is supplemented by SE imaging and EDS, which are necessary for the quantification of phase models used in the Rietveld analysis, in addition to offering cross-validation of the neutron diffraction results. Given the elemental composition of the IN718 powder and the potential stoichiometries of all phases, mass balance calculations showed that the experimentally determined phase compositions are plausible. The main conclusions of this study are:

- Considering that the LPBF material has much higher δ and much less of γ'' content than the wrought material, it is inferred that the LPBF process creates microstructural conditions that promote the transformation from γ'' to δ during the AMS 5663 heat-treatment. Moreover, the δ phase in the LPBF material is found to be much smaller and is located at both grain boundaries and within grains, as opposed to the wrought material where it is coarse and intergranular.
- Treatment by HIP after LPBF creates a material with a much lower content of δ phase and a higher content of γ'' phase after the AMS 5663 heat-treatment as compared to the LPBF material in the same condition. LPBF + HIP phase composition is similar to that of the wrought material, but has slightly smaller δ and MC particle sizes contributing to more dispersion strengthening.
- Despite having lower γ'' content, the LPBF material is stronger than both LPBF + HIP and wrought materials. Such behavior is rationalized by the finer grain structure in the LPBF material, as opposed to the LPBF + HIP and wrought materials, in addition to the presence of ~200 nm MC precipitates that also contribute to dispersion hardening. The final grain structure in the LPBF material is influenced by the presence of finer, more dispersed δ precipitates.

Data availability

The raw/processed data required to reproduce these findings cannot be shared at this time due to technical or time limitations.

Declaration of competing interest

The authors declare that they have no known competing financial interests or personal relationships that could have appeared to influence the work reported in this paper.

CRediT authorship contribution statement

Nicholas C. Ferreri: Formal analysis, Investigation, Methodology, Software, Validation, Writing - original draft. **Sven C. Vogel:** Data curation, Formal analysis, Methodology, Resources, Supervision, Writing - review & editing. **Marko Knezevic:** Conceptualization, Funding acquisition, Methodology, Project administration, Resources, Supervision, Writing - review & editing.

Acknowledgments

This research was sponsored by the U.S. National Science Foundation and was accomplished under the CAREER grant no. CMMI-1650641.

References

[1] W.F. Smith, Structure and Properties of Engineering Alloys, McGraw-Hill, New York, 1981.
[2] A.K. Misrta, D. Whittenberger, Fluoride salts and container materials for thermal energy storage applications in the temperature range 973 to 1400 K, in: 22nd Intersociety Energy Conversion Engineering Conference, 1987.
[3] J.R. Davis, ASM Specialty Handbook: Heat-Resistant Materials, ASM International, 1997.
[4] H.E. D, Progress in additive manufacturing, JOM 67 (2015) 580–581.
[5] S. Safdar, A.J. Pinkerton, L. Li, M.A. Sheikh, P.J. Withers, An anisotropic enhanced thermal conductivity approach for modelling laser melt pools for Ni-base super alloys, Appl. Math. Model. 37 (2013) 1187–1195.

[6] M. Knezevic, B.K. Chun, J.Y. Oh, W.T. Wu, R.A. Ress Iii, M.G. Glavicic, S. Srivatsa, Modeling machining distortion using the finite element method: application to engine disk 40 (2012) 40–46.
[7] W.E. Frazier, Metal additive manufacturing: a review, J. Mater. Eng. Perform. 23 (2014) 1917–1928.
[8] E.C. Santos, M. Shiomi, K. Osakada, T. Laoui, Rapid manufacturing of metal components by laser forming, Int. J. Mach. Tool Manufact. 46 (2006) 1459–1468.
[9] D.D. Gu, W. Meiners, K. Wissenbach, R. Poprawe, Laser additive manufacturing of metallic components: materials, processes, and mechanisms, Int. Mater. Rev. 57 (2013) 133–164.
[10] H. Zare, M. Jahedi, M.R. Toroghinejad, M. Meratian, M. Knezevic, Compressive, shear, and fracture behavior of CNT reinforced Al matrix composites manufactured by severe plastic deformation, Mater. Des. 106 (2016) 112–119.
[11] T.J. Barrett, M. Knezevic, Modeling material behavior during continuous bending under tension for inferring the post-necking strain hardening response of ductile sheet metals: application to DP 780 steel, Int. J. Mech. Sci. 174 (2020), 105508.
[12] T.J. Barrett, M. Knezevic, Deep drawing simulations using the finite element method embedding a multi-level crystal plasticity constitutive law: experimental verification and sensitivity analysis, Comput. Methods Appl. Mech. Eng. 354 (2019) 245–270.
[13] D.W. Brown, D.P. Adams, L. Balogh, J.S. Carpenter, B. Clausen, G. King, B. Reedlunn, T.A. Palmer, M.C. Maguire, S.C. Vogel, In situ neutron diffraction study of the influence of microstructure on the mechanical response of additively manufactured 304L stainless steel, Metall. Mater. Trans. 48 (2017) 6055–6069.
[14] B.E. Carroll, T.A. Palmer, A.M. Beese, Anisotropic tensile behavior of Ti-6Al-4V components fabricated with directed energy deposition additive manufacturing, Acta Mater. 87 (2015) 309–320.
[15] N.C. Ferreri, S. Ghorbanpour, S. Bhowmik, R. Lussier, J. Bicknell, B.M. Patterson, M. Knezevic, Effects of build orientation and heat treatment on the evolution of microstructure and mechanical properties of alloy Mar-M-509 fabricated via laser powder bed fusion, Int. J. Plast. 121 (2019) 116–133.
[16] Z. Wang, T.A. Palmer, A.M. Beese, Effect of processing parameters on microstructure and tensile properties of austenitic stainless steel 304L made by directed energy deposition additive manufacturing, Acta Mater. 110 (2016) 226–235.
[17] A.D. Kudzal, B.A. McWilliams, J. Taggart-Scarff, M. Knezevic, Fabrication of a low alloy ultra-high strength (>1500 MPa yield) steel using powder bed fusion additive manufacturing, Mater. Sci. Eng. 770 (2020), 138512.
[18] M. Jahedi, M. Knezevic, M. Paydar, High-pressure double torsion as a severe plastic deformation process: experimental procedure and finite element modeling, J. Mater. Eng. Perform. 24 (2015) 1471–1482.
[19] M. Cloots, K. Kunze, P. Uggowitzer, K. Wegener, Microstructural characteristics of the nickel-based alloy IN738LC and the cobalt-based alloy Mar-M509 produced by selective laser melting, Mater. Sci. Eng. A 658 (2016) 68–76.
[20] C.A. Bronkhorst, J.R. Mayeur, V. Livescu, R. Pokharel, D.W. Brown, G.T. Gray, Structural representation of additively manufactured 316L austenitic stainless steel, Int. J. Plast. 118 (2019) 70–86.
[21] M. Knezevic, S. Ghorbanpour, Response of Inconel 718 Using a crystal plasticity model incorporating the effects of precipitates, in: Proceedings of the 9th International Symposium on Superalloy 718 & Derivatives: Energy, Aerospace, and Industrial Applications, 2018, pp. 655–668.
[22] R. Jiang, A. Mostafaei, J. Pauza, C. Kantzos, A.D. Rollett, Varied heat treatments and properties of laser powder bed printed Inconel 718, Mater. Sci. Eng. 755 (2019) 170–180.
[23] R.E. Smallman, A.H.W. Ngan, Modern Physical Metallurgy, eighth ed., Elsevier/Butterworth-Heinemann, Oxford ; Waltham, MA, 2014.
[24] D.A. Porter, K.E. Easterling, M.Y. Sherif, Phase Transformations in Metals and Alloys, third ed., CRC Press, Boca Raton, FL, 2009.
[25] A. Thompson, J. Knott, Micromechanisms of brittle fracture, Metall. Trans. 24 (1993) 523–534.
[26] A. Weronski, T. Hejwowski, Thermal Fatigue of Materials, Marcel Dekker, Inc., New York, 1991.
[27] W.J. Sames, K.A. Unocic, R.R. Dehoff, T. Lolla, S.S. Babu, Thermal effects on microstructural heterogeneity of Inconel 718 materials fabricated by electron beam melting, J. Mater. Res. 29 (2014) 1920–1930.
[28] H. Qi, M. Azer, A. Ritter, Studies of standard heat treatment effects on microstructure and mechanical properties of laser net shape manufactured INCONEL 718, Metall. Mater. Trans. 40 (2009) 2410–2422.
[29] R.B. Li, M. Yao, W.C. Liu, X.C. He, Isolation and determination for delta, gamma prime, and gamma double prime phases in inconel 718 alloy, Scripta Mater. 46 (2002) 635–638.
[30] C.H. Lund, Physical Metallurgy of Nickel-Base Superalloys, Defense Metals Information Center, 1961.
[31] S. Mahadevan, S. Nalawade, J.B. Singh, A. Verma, B. Paul, K. Ramaswamy, Evolution of Delta Phase Microstructure in Alloy 718, TMS, 2010, pp. 737–750.
[32] D. Mukherji, R. Gilles, B. Barbier, D. Del Genovese, B. Hasse, P. Struntz, T. Wroblewski, H. Fuess, J. Rosler, Lattice misfit measurement in Inconel 706 containing coherent gamma prime and gamma double prime precipitates, Scripta Mater. 48 (2003) 333–339.
[33] M. Sundararaman, P. Mukhopadhyay, S. Banerjee, Precipitation of the delta-Ni3Nb phase in two nickel base superalloys, Metall. Trans. 19A (1988) 453–465.
[34] M. Dehmas, J. Lacaze, A. Niang, B. Viguier, TEM study of high-temperature precipitation of delta phase in inconel 718 alloy, Adv. Mater. Sci. Eng. 2011 (2011) 1–9.
[35] H.Y. Zhang, S.H. Zhang, M. Cheng, Z. Zhao, Microstructure evolution of IN718 alloy during the delta process, in: International Conference on the Technology of Plasticity. Cambridge, United Kingdom, 2017, pp. 1099–1104.
[36] K.N. Amato, S.M. Gaytan, L.E. Murr, E. Martinez, P.W. Shindo, J. Hernandez, S. Collins, F. Medina, Microstructures and mechanical behavior of Inconel 718 fabricated by selective laser melting, Acta Mater. 60 (2012) 2229–2239.
[37] S. Gribbin, J. Bicknell, L. Jorgensen, I. Tsukrov, M. Knezevic, Low cycle fatigue behavior of direct metal laser sintered Inconel alloy 718, Int. J. Fatig. 93 (2016) 156–167.
[38] S. Ghorbanpour, M.E. Alam, N.C. Ferreri, A. Kumar, B.A. McWilliams, S.C. Vogel, J. Bicknell, I.J. Beyerlein, M. Knezevic, Experimental characterization and crystal plasticity modeling of anisotropy, tension-compression asymmetry, and texture evolution of additively manufactured Inconel 718 at room and elevated temperatures, Int. J. Plast. 125 (2020) 63–79.
[39] H.R. Wenk, L. Lutterotti, S.C. Vogel, Texture analysis with the new HIPPO TOF diffractometer, Nucl. Instrum. Methods Phys. Res. Sect. A Accel. Spectrom. Detect. Assoc. Equip. 515 (2003) 575–588.
[40] V.F. Sears, Neutron scattering lengths and cross sections, Neutron News 3 (1992) 26–37.
[41] W.H. McMaster, N.K. Del Grande, J.H. Mallett, J.H. Hubbell, Compilation of X-Ray Cross Sections, Lawrence Livermore Radiation Lab, California University, 1969.
[42] M. Zecevic, M. Knezevic, A new visco-plastic self-consistent formulation implicit in dislocation-based hardening within implicit finite elements: application to high strain rate and impact deformation of tantalum, Comput. Methods Appl. Mech. Eng. 341 (2018) 888–916.
[43] M. Zecevic, M. Knezevic, Latent hardening within the elasto-plastic self-consistent polycrystal homogenization to enable the prediction of anisotropy of AA6022-T4 sheets, Int. J. Plast. 105 (2018) 141–163.
[44] M. Zecevic, I.J. Beyerlein, M. Knezevic, Coupling elasto-plastic self-consistent crystal plasticity and implicit finite elements: applications to compression, cyclic tension-compression, and bending to large strains, Int. J. Plast. 93 (2017) 187–211.
[45] M. Zecevic, M. Knezevic, An implicit formulation of the elasto-plastic self-consistent polycrystal plasticity model and its implementation in implicit finite elements, Mech. Mater. 136 (2019), 103065.
[46] M. Zecevic, M. Knezevic, A dislocation density based elasto-plastic self-consistent model for the prediction of cyclic deformation: application to Al6022-T4, Int. J. Plast. 72 (2015) 200–217.
[47] S. Ghorbanpour, M. Zecevic, A. Kumar, M. Jahedi, J. Bicknell, L. Jorgensen, I. J. Beyerlein, M. Knezevic, A crystal plasticity model incorporating the effects of precipitates in superalloys: application to tensile, compressive, and cyclic deformation of Inconel 718, Int. J. Plast. 99 (2017) 162–185.
[48] EOS NickelAlloy IN718 Data Sheet, EOS GmbH - Electro Optical Systems, 2014.
[49] S.H. Chang, S.C. Lee, T.P. Tang, H.H. Ho, Influences of soaking time in hot isostatic pressing on strength of inconel 718 superalloy, Mater. Trans. 47 (2006), 526-432.
[50] J. Schneider, B. Lund, M. Fullen, Effect of heat treatment variations on the mechanical properties of Inconel 718 selective laser melted specimens, Add. Manufact 21 (2018) 248–254.
[51] M. Jahedi, B.A. McWilliams, M. Knezevic, Deformation and fracture mechanisms in WE43 magnesium-rare earth alloy fabricated by direct-chill casting and rolling, Mater. Sci. Eng. 726 (2018) 194–207.
[52] M. Jahedi, B.A. McWilliams, P. Moy, M. Knezevic, Deformation twinning in rolled WE43-T5 rare earth magnesium alloy: influence on strain hardening and texture evolution, Acta Mater. 131 (2017) 221–232.
[53] M. Jahedi, B.A. McWilliams, F.R. Kellogg, I.J. Beyerlein, M. Knezevic, Rate and temperature dependent deformation behavior of as-cast WE43 magnesium-rare earth alloy manufactured by direct-chill casting, Mater. Sci. Eng. 712 (2018) 50–64.
[54] EDAX Standardless Quant Metods vol. 17, EDAX Insight, 2019, pp. 1–9.
[55] J.F. Radavich. Metallography of a High Strength Modified 718 Alloy-PWA 1472. Superalloys 718, 625 and Various Derivatives. p.865-877.
[56] P.W. Lisowski, K.F. Schoenberg, The Los Alamos neutron science center, Nucl. Instrum. Methods Phys. Res. Sect. A Accel. Spectrom. Detect. Assoc. Equip. 562 (2006) 910–914.
[57] A.S. Losko, S.C. Vogel, H.M. Reiche, H. Nakotte, A six-axis robotic sample changer for high-throughput neitron powder diffraction and texture measurements, J. Appl. Crystallogr. 47 (2014) 2109–2112.
[58] J.M. Alves, L.P. Brandao, A. dos Santos Paula, The influence of sample preparation on the quantitative analysis of the volume fraction of martensite formed in a 304L trip steel, Mater. Res. 18 (2015).
[59] S. Matthies, L. Lutteroti, H.R. Wenk, Advances in texture analysis from diffraction spectra, J. Appl. Crystallogr. 30 (1997) 31–42.
[60] L. Lutterotti, S. Matthies, H.R. Wenk, A.S. Schultz, J.W. Richardson, Combined texture and structure analysis of deformed limestone from time-of-flight neutron diffraction data, J. Appl. Phys. 81 (1996) 594–600.
[61] B.D. Cullity, Elements of X-Ray Diffraction, 2 ed., Anderson-Wesley Publishing Company, 1978.
[62] L. Lutterotti, P. Scardi, Simultaneous structure and size-strain refinement by the Rietveld method, J. Appl. Crystallogr. 23 (1990) 246–252.
[63] M. Ferrari, L. Lutterotti, Method for the simultaneous determination of anisotropic residual stresses and texture by x-ray diffraction, J. Appl. Phys. 76 (1994) 7246–7255.
[64] T.J. Barrett, A. Eghtesad, R.J. McCabe, B. Clausen, D.W. Brown, S.C. Vogel, M. Knezevic, A generalized spherical harmonics-based procedure for the interpolation of partial datasets of orientation distributions to enable crystal mechanics-based simulations, Materialia 6 (2019) 100328.

[65] M. Knezevic, I.J. Beyerlein, D.W. Brown, T.A. Sisneros, C.N. Tomé, A polycrystal plasticity model for predicting mechanical response and texture evolution during strain-path changes: application to beryllium, Int. J. Plast. 49 (2013) 185–198.
[66] M. Knezevic, R.A. Lebensohn, O. Cazacu, B. Revil-Baudard, G. Proust, S.C. Vogel, M.E. Nixon, Modeling bending of α-titanium with embedded polycrystal plasticity in implicit finite elements, Mater. Sci. Eng. 564 (2013) 116–126.
[67] M. Zecevic, M. Knezevic, I.J. Beyerlein, C.N. Tomé, An elasto-plastic self-consistent model with hardening based on dislocation density, twinning and de-twinning: application to strain path changes in HCP metals, Mater. Sci. Eng. 638 (2015) 262–274.
[68] R.I. Todd, M.A.M. Bourke, C.E. Borsa, R.J. Brook, Neutron diffraction measurements of residual stresses in alumina/SiC nanocomposites, Acta Mater. 45 (1997) 1791–1800.
[69] M. Morinaga, K. Sone, T. Kamimura, K. Ohtaka, N. Yukawa, X-ray determination of static displacements of atoms in alloyed Ni3Al, J. Appl. Crystallogr. 21 (1988) 41–46.
[70] L.M. Peng, G. Ren, S.L. Dudarev, M.J. Whelan, Debye-Waller factors and absorptive scattering factors of elemental crystals, Acta Crystallogr. 52A (1996) 456–470.
[71] P.V. Mohan Rao, K. Satyanarayana Murthy, S.V. Suryanarayana, X-ray determination of Debye-Waller factors and order parameters of Ni3Al Alloys, J. Appl. Crystallogr. 26 (1993) 670–676.
[72] R.A. Young, The Rietveld Method, International Union of Crystallography, 1993.
[73] S. Takajo, S.C. Vogel, Determination of pole figure coverage for texture measurements with neutron time-of-flight diffractometers, J. Appl. Crystallogr. 51 (2018) 895–900.
[74] A. Devaux, L. Naze, R. Molins, A. Pineau, A. Organista, J.Y. Guedou, J.F. Uginet, P. Heritier, Gamma double prime precipitation kinetic in alloy 718, Mater. Sci. Eng. A 486 (2008) 117–122.
[75] S. Azadian, L.Y. Wei, R. Warren, Delta phase precipitation in Inconel 718, Mater. Char. 53 (2004) 7–16.
[76] B.H. Toby, R factors in Rietveld analysis: how good is good enough? Powder Diffr. 12 (2006) 67–70.
[77] K. Lohnert, F. Pyczak, Microstructure Evolution in the Nickel Base Superalloy Allvac718Plus, TMS, 2010, pp. 877–891.
[78] P.M. Mignanelli, N.G. Jones, E.J. Pickering, O.M.D.M. Messe, C.M.F. Rae, M. C. Hardy, H.J. Stone, Gamma-gamma prime-gamma double prime dual-superlattice superalloys, Scripta Mater. 136 (2017) 136–140.
[79] S.I. Kwon, S.H. Bae, J.H. Do, C.Y. Jo, H.U. Hong, Characterization of the microstructures and the cryogenic mechanical properties of electron beam welded Inconel 718, Metall. Mater. Trans. 47 (2016) 777–787.
[80] B. Hassan, J. Corney, Grain boundary precipitation in inconel 718 and ATI 718 plus, Mater. Sci. Technol. 33 (2017) 1879–1889.
[81] G.A. Knorovsky, M.J. Cieslak, T.J. Headley, A.D. Romig, W.F. Hammetter, Inconel 718: a solidification diagram, Metall. Trans. 20A (1987) 2149–2158.
[82] A. Mostafa, I.P. Rubio, B. Brailovski, M. Jahazi, M. Medraj, Structure, texture, and phases in 3D printed IN718 alloy subjected to homogenization and HIP treatments, Metals 7 (2017).
[83] Y. Zhu, S. Zhang, T. Zhang, L. Lou, Y. Tong, X. Ning, Z. Hu, X. Xie, in: E.A. Loria (Ed.), Effect of P, S, B, and Si on the Solidification Segregation of Inconel 718 Alloy, TMS, 1994.
[84] J.T. Guo, L.Z. Zhou, in: R.D. Kissinger (Ed.), The Effect of Phosphorus, Sulfur, and Silicon on Segregation, Solidification and Mechanical Properties of Cast Alloy 718, TMS, 1996.
[85] M. Jahedi, E. Ardjmand, M. Knezevic, Microstructure metrics for quantitative assessment of particle size and dispersion: application to metal-matrix composites, Powder Technol. 311 (2017) 226–238.
[86] S. Gribbin, S. Ghorbanpour, N.C. Ferreri, J. Bicknell, I. Tsukrov, M. Knezevic, Role of grain structure, grain boundaries, crystallographic texture, precipitates, and porosity on fatigue behavior of Inconel 718 at room temperature and elevated temperatures, Mater. Char. 149 (2018) 184–197.
[87] B. Kad, P. Hazzledine, Monte Carlo simulations of grain growth and Zener pinning, Mater. Sci. Eng. A 238 (1997) 70–77.
[88] N. Hansen, Hall-Petch relation and boundary strengthening, Scripta Mater. 51 (2004) 801–806.